1.4.6.5 Volume of Aadsorbed Water Molecules on the Inner Surface in the Water-filled Pore Area

In Section 1.4.7, results of experimental investigations and molecular-dynamic (MD) studies are reproduced on the question of adsorbed water-molecule films at the inner surface in the water-filled pore region.

Reported are, among others, the results of capillary water transport experiments on nanopores, according to which stable surface films of 0.4–0.6 [nm] thickness (Xu et al. [54]) or 0.60 [nm] thickness (Gruener et al. [55]) are formed on the inner surfaces of the pores. These adsorbed films constrict the pore cross sections and do not themselves participate in fluid transport.

K. Wu et al. [56**] evaluates 50 corresponding studies and finds a nonparticipating film thickness of about 0.7 [nm] and a "dramatic" increase in viscosity** of the adsorbed films at pore diameters ≤ 1.4 [nm].

Antognozzi et al. [57], Zhao et al. [53], and Arai et al. [58] determine using AFM that tough molecular layers of at least 0.70 [nm] form on surfaces with behavior different from bulk water.

The theoretical consideration undertaken in Section 1.4.6.4 based on the surface energy of adsorbed films yields a sorption thickness between 2.5 and 4.4 molecular layers, on average order of magnitude 0.90 [nm].

Knowing the sorption film thicknesses in the water-filled pore regions is of high importance for understanding and modeling moisture transport in porous materials. Therefore, for the sample material REF, it was computationally determined which water content fraction results in partial or complete water saturation of the material, if constant adsorption film thicknesses are taken as a basis in the order of magnitude of the previously mentioned, experimentally and theoretically determined values.

Film thicknesses $t_{film} = 0.30$, 0.45, and $0.60 \cdot 10^{-9} = \text{const.}$ [m] were used in the calculation.

The following relation was used for this purpose:

$$\Delta V_{film}(\varphi_1) = \theta_N(\varphi_0) + t_{film} \cdot \Delta A(\varphi_0, \varphi_1) \tag{1.98}$$

Then, to an initial value $\theta_N(\varphi_0)$ is added the water volume, which is the product of the film thickness t_{film} and the inner surface area $\Delta A(\varphi_0, \varphi_1)$ between the initial φ_0 and the running upper φ_1 boundaries. $\theta_N(\varphi_0)$ is the water content of the net adsorption curve at a pore radius of a water molecule $r_R(\varphi_0) = 0.30 \cdot 10^{-9}$ with $\varphi_0 = 0.0116$. $\Delta A(\varphi_0, \varphi_1)$ corresponds to the area integral (1.77).

For smaller φ values, the volume from film thickness and surface area partially exceeds the existing pore volume. It is then set equal to the corresponding volume of the net storage function.

The result of the calculations can be seen in Figure 1.35. It can be seen that for a film thickness of 0.30 [nm], the pores are filled with adsorbed water up to $\varphi \approx 20\%$, for a film thickness of 0.45 [nm] up to $\varphi \approx 40\%$, and for a film thickness of 0.60 [nm] at relative air humidity up to $\varphi \approx 55\%$. These conditions have an appreciable effect on moisture storage and transport in a pore system, which must be taken into account when modeling moisture transport.

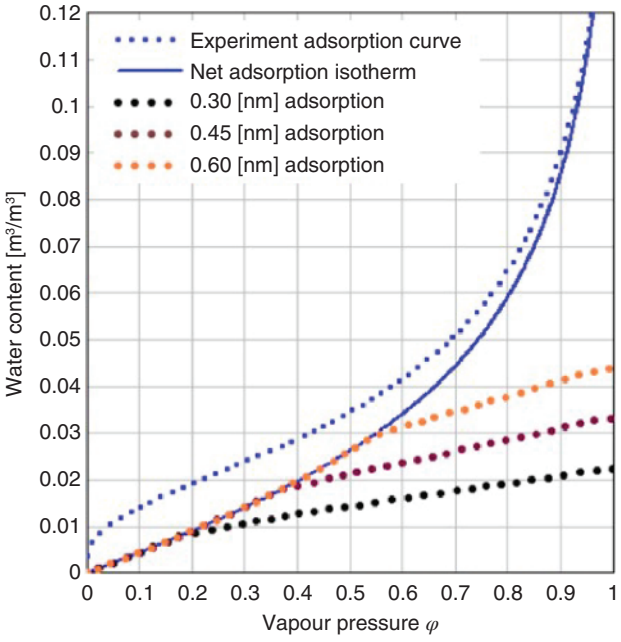

Figure 1.35 Adsorption isotherm of the material REF and net storage function and volume of adsorbed water molecules at the inner surface **in the water-filled pore region** with film thicknesses of 0.30, 0.45, and 0.60 [nm]. **The net adsorption isotherm** shows the water content of the pore system up to the considered value φ, without the moisture content adsorbed on the inner surface in the non-filled pore area above.

1.4.7 Molecular Simulations and Experimental Investigations on the Dimension of Adsorbed Film Thicknesses (International Research Results)

With the help of computer programs, that simulate via modeling, the interactions between molecules and atoms to their motions, mergers and attachments, it is possible to estimate the sorption of liquids on solids or resulting film thicknesses. For years, programs have been used for this purpose, known as **MD or MDS** as molecular dynamics simulations, which are further developed for simultaneous description of chemical reactions under the name molecular mechanics, in the last stage as **reactive molecular dynamics (RMD)**, which obviously require very large computational effort, for example, require the use of parallel computers, compare H.M. Aktulga et al. [59]. An overview of the state of development and available programs is given by K. Farah et al. [60].

Castrillon et al. [61] reports in his paper the results of **MD simulations** on sorption of water films on quartz surfaces. Among other things, the distribution of density and local potential energy near the surface is also reported. Castrillon, extending his calculations to water molecule thicknesses corresponding to about 15 monolayers, finds an influence on the water-molecule orientation up to a distance

of about 1.4 [nm] from the surface and **a firmer bond or stiffness (H-bonding) of the water-molecule layers up to a thickness of 0.4–0.6 [nm].**

However, the results of calculations with current computer programs always require confirmation by the results of experimental investigations:

The development of AFM or surface force apparatus (SFA) technique now allows additional insight into the formation of film thicknesses at interfaces. The paper by Israelachvili et al. [62] provides an overview of the status of this development up to 2010. In these devices, an upper tip (guided by special piezoelectric crystals) is gradually moved in small air-conditioned chambers to the material surface to be tested, which may be covered with a liquid film thickness. The exact distances are measured using light wavelengths or laser technology.

Figure 1.36 shows schematically the structure of an AFM. The caption provides more information about the function. A recent overview of the state of AFM technique can be found from Peng et al. [63]. Problems concerning the interpretation of the results of conventional AFM technique with tip insertion are discussed in [64]. An overview of other investigation techniques used, such as NMR and X-ray techniques, can be found in Monroe et al. [65].

In the work of Xu et al. [54], permeability experiments and subsequent MD simulations are reported. In particular, transport experiments are performed on fine porous material of Vycor glass with mean pore diameters of 3.4 and 7.2 [nm] and on porous quartz material Xerogel with mean pore diameters of 3.4 [nm]. Aqueous solutions with 1M NaCl and 1M $CaCl_2$ are also used for comparison.

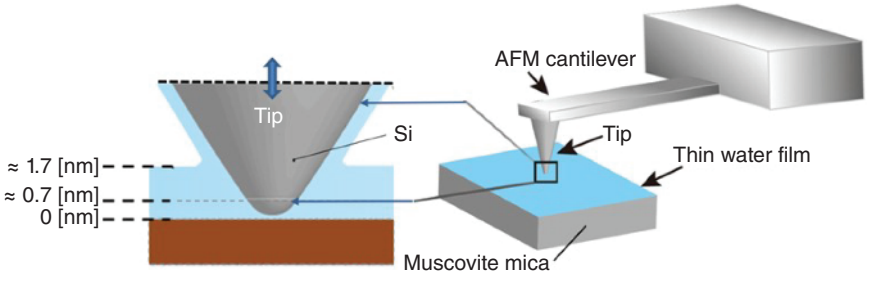

Figure 1.36 Schematic representation of the principle of an AFM (atomic force microscope) inside a temperature and humidity adjustable measuring chamber. A very fine tip attached to a cantilever is moved over the area of the interface to be measured, horizontally in 2D or/and vertically in 3D scanning. The tip or curved surface can be guided into the liquid film in Ångström steps. The path of the tip is measured by a laser apparatus or a light wave interference system, and the ultra-small forces occurring at the tip are measured via the spring stiffness of the cantilever. The cantilever can also operate above the interface with the solid submerged in the liquid. The cantilever can be operated in static mode or in dynamic mode (near its resonance frequency), in the latter case frequency-modulated as FM-AFM or amplitude-modulated as AM-AFM. Source: The pictorial elements shown here are taken from Arai et al. [58]/Springer Nature/CC BY 4.0. The measurements of Arai et al. were made in saturated water vapor atmosphere on interface to muscovite mica. The nanometer dimensions given in the figure are measurement results: up to about 0.7 [nm] a tough molecular layer was measured, covered up to about 1.7 [nm], with bulk water.

In both the experiments and the MD simulations, respectively, it is found that the material pores have a 2-layer water-molecule film of about 0.6 [nm], which leads to a corresponding narrowing of the pores during moisture transport. There were no significant changes when sodium chloride and calcium chloride solutions were used.

S. Gruener et al. [55] perform capillary water uptake experiments on Vycor glass with mean pore diameters of 3.4 and 4.9 [nm]. The analyses revealed surface films not participating in moisture transport on the order of 2 molecule layers.

Asay and Kim [66] performs infrared spectroscopic ATR (attenuated total reflection) studies on flat silicate surfaces at 20 °C and increases the relative humidity of air and finds that an approximately 3 monolayer thick water film of an "icelike" nature forms on the silicate surface.

K. Wu et al. [56] evaluates the results of more than 50 different studies on the question of the formation of water-film thickness using a model based on Hagen-Poiseuille's theory to describe water transport in cylindrical pores in the presence of film thicknesses on the inner pore walls. The theory is applicable to pore diameters >1.4 [nm], since a dramatic increase in viscosity occurs for smaller diameters. Wu's comparative calculations lead to the conclusion that, especially for pore diameters <10 [nm], there is an increase in viscosity for hydrophilic materials compared to bulk water, while a large decrease in transport resistance occurs for transport processes in hydrophobic materials. In hydrophilic materials, according to Wu, an approximately 0.7 [nm]-thick stable film thickness is formed on the inner surfaces.

Antognozzi et al. show in [57] results of measurements on thickness-dependent shear viscosity on a glass/mica combination, determined with a transverse dynamic force microscope **(TDFM)**. A section of an optical glass fiber with plane-cut surfaces is used as a tip and guided in dynamic shear motions over water films of different thicknesses on a muscovite mica surface. The experiments show, that below about 0.9 [nm], there is a dramatic increase in shear viscosity or shear stiffness of the water-molecule layers between the glass surface and the mica.

This increase in stiffness therefore occurs below a film thickness of 0.45 [nm] with respect to one of the two material surfaces.

Figure 1.37 shows AFM results and MD calculations from Kimura et al. [67]. These analyses were performed at the interface between muscovite mica and an upstanding 1M KCl aqueous solution. According to the results of Martin-Jimenez et al. [68], ion concentrations ≤ 1M have only a minor influence on the structure of the water-molecule layers, compare the following remarks. From the results shown in **Figure 1.37**, it can be concluded that a film thickness of 0.45 [nm] was also present, according to the results of Antognozzi et al. From these results, it can be concluded that, at least for low-concentrated electrolyte solutions (or pure water), a primary sorption layer thickness of about 0.45 [nm], already determined by Kimura et al. and Antognozzi et al., can be assumed. Furthermore, it follows from the present work that primary layers of greater thickness result at higher electrolyte concentrations.

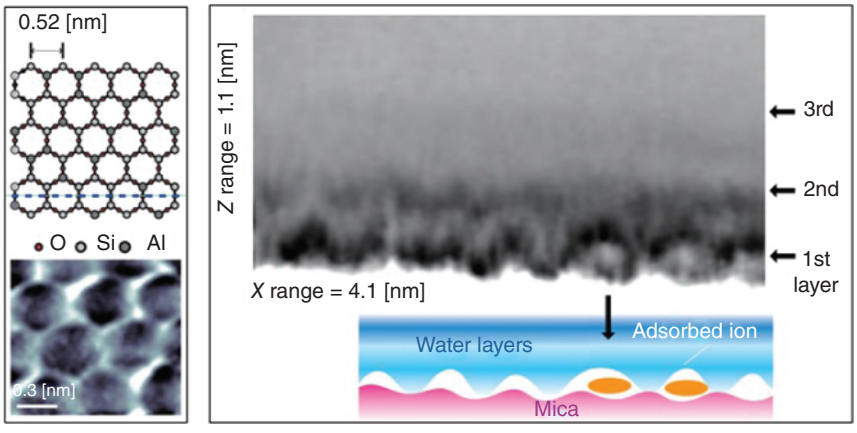

Figure 1.37 Results of 2D force scanning of the muscovite mica material interface perpendicularly into the overlying 1M KCl aqueous solution using FM-AFM. **The left part** schematically shows the crystalline structure of the mica. Below is the microscopic AFM image of the corresponding surface when scanning the surface. This cleaved mica surface corresponds to a structural section corresponding to the blue-dashed line in the schematic structure image above. **The right part** shows the registered structure in the aqueous solution above the mica surface. At the muscovite mica/water interface, the water molecule layer penetrates into the center of the hexagonal structure schematically illustrated on the left. In the upper layers, fluid water molecule layers are observed, and they show a smaller correlation with the surface structure. The layers registered by the authors are indicated at the right edge of the image. The total image height is 1.1 [nm]. The yellow particles in the sub-image are likely to be K^+ ions or hydrated K^+ ion complexes adsorbed on the surface. Source: Kimura et al. [67]/AIP Publishing.

By Martin-Jimenez et al. [68] present further insightful investigation results on 3D structure at interfaces. **Figure 1.38** contains some results of these investigations and related details. Further results of this work can be reproduced as follows:

The interaction with the mica is found to have a nearly complete monolayer of cations at low salt concentrations (0.2M), as indicated by the AFM images. The K^+ ions from the solution occupy the positions in the cleaved plane previously occupied by K^+ ions in the bulk mica crystal. The water molecules from the first hydration layer are tightly bound to the solid surface, occupying the space between the cations. The second hydration layer is placed 0.25 [nm] above the adsorbed K^+ ions and it follows its atomic corrugation. The water molecules in the 2nd layer are centered on top of the cations of the first layer, but with a larger lateral spreading. The accompanying DFC simulation predictions show a significant reduction of the cation coverage of the mica at low salt concentration.

At higher salt concentrations (3–5M), the interfacial layer has a different structure and composition. It is thicker and shows a crystal-like structure.

The observed phenomenology is not restricted to KCl solutions. It also applies to other alkali halide electrolyte solutions.

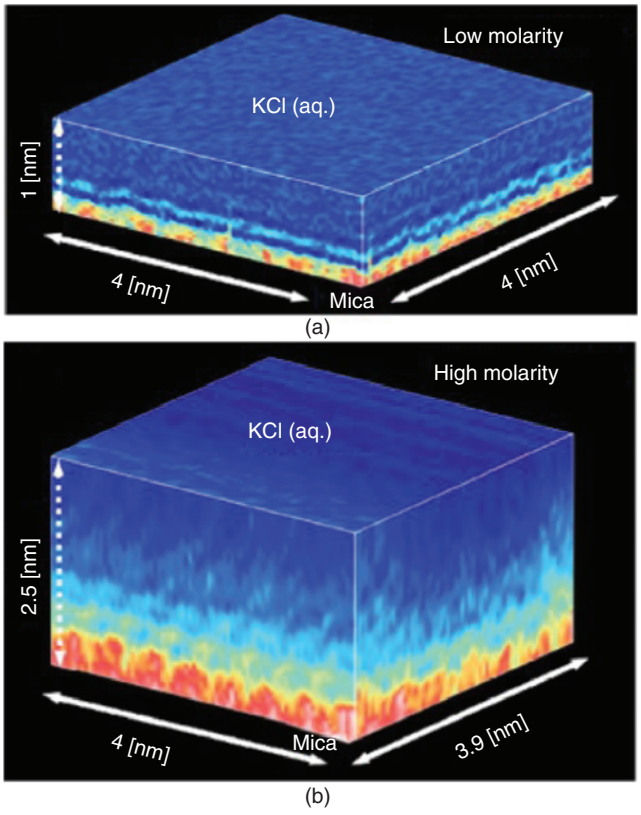

Figure 1.38 Three-dimensional AFM-images of muscovite mica/electrolyte solution Interfaces. (a) 3D AFM image of a KCl (aq.) solution (0.2M KCl). The image shows a monolayer resp. interface of partial adsorbed K^+ ions (light red) topped by two hydration layers (lighter stripes), following the atomic corrugation of the mica surface. (b) 3D AFM image of a mica-KCl (aq.) interface (4M KCL). The interface is divided into two main regions: an ordered liquid layer extending up to 2 [nm] from the mica surface into the bulk solution above it. These 3D maps show the variations of the phase shift of the tip's oscillation. The 3D AFM experiments were performed at 300 K. Source: Martin-Jimenez et al. [68]/Springer Nature.

The results reported by G. Zhao et al. in [53] are particularly remarkable as well. **Figure 1.39a,b** shows selected results of the investigations with a SFA 2000 apparatus.

These AFM investigations have the special feature that the conventional tip configuration was not used, but instead 2 cylindrical surfaces (tube sections with a radius of 2 [cm]) were arranged in a crossed configuration opposite each other. Both crossed cylindrical surfaces were covered with a cleaved layer of muscovite mica. The mutual distance of both surfaces was measured in the AFM in steps of 0.1 [nm] using the MBI lightwave interference technique FECO, using a video camera to allow direct monitoring of the surface separation and phase change of the adsorbed water between two mica surfaces. More Details of the measurements

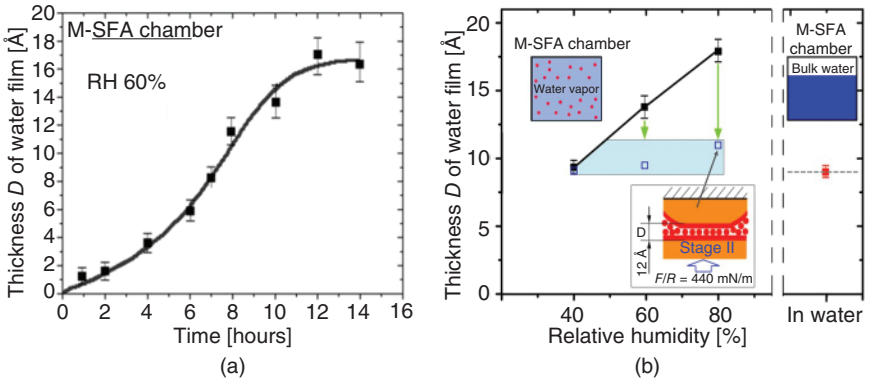

Figure 1.39 Measurement results of G. Zhao et al. from [53] **on water vapor sorption on muscovite** mica (measured with SFA 2000 measuring apparatus). (a) Time-dependent evolution of sorption film thickness from water on muscovite mica under constant vapor pressure. (b): The black squares give the measured values of the formed film thicknesses as a function of vapor pressure at sufficient distance of the opposing surfaces. When the surfaces are automatically moved together, part of the original water film is reduced. This process comes to a halt due to corresponding counterforce at a mutual distance of the muscovite surfaces in the order of $D = 0.90$ [nm] after 10 hours, which leads to a layer thickness of $D/2 = 0.45$ [nm] related to each of the two surfaces, if the feed force is not significantly increased. The solid square symbols indicate the initial thickness of the measured adsorbed water film at the moment of two mica surfaces contacting together. The hollow square symbols indicate the film thickness reduced to the light blue area under the action of the external load schematically shown by the sub-picture below. **In the right part of the figure (b)** the corresponding measured value of approx. 0.9 [nm] after approx.10 hours pressure at 80% RH results, when the experiment is carried out **in water**. This result also corresponds to an individual layer thickness of 0.45 [nm] per surface. Source: Zhao et al. [53]/AIP Publishing.

can be taken from **Figure 1.39b** or the corresponding figure caption. Some relevant details will be presented here in addition:

After vapor adsorption process, over hours at sufficient distance between the mica surfaces, the opposing mica surfaces are pressed together with the pressure value mentioned in the sub-figure of **Figure 1.39b**. A film of water molecules of thickness of about 0.45 [nm] is formed under this pressure. The authors describe the state of this film as similar to solid that cannot flow easily.

In following experiments, the stability of this film under sustained compression was tested. It is found that creeping occurs at which after hours, the layer thickness was reduced approximately to half. They conclude that the primary layer (of 0.45 [nm]) of the adsorbed water is unstable under the action of an external load and its property is similar to an ice-crystal structure that will creep under the action of an external load even with a smaller pressure.

Separation tests after compression were also performed. In this case, the separation between two rigid solid surfaces happens without any capillary condensation. It is found that the adhesion force increases with the relaxation time when the mica surfaces are bridged by the first layer of the adsorbed water film.

Figure 1.39a shows the results of time-dependent adsorption experiments: after 10 hours at 60% RH/25 °C an adsorption layer thickness of $D/2 \approx 0.70$ [nm] was formed on the mica surface due to the vapor pressure in the test chamber. These results on 12 independent measurements, each with new muscovite surfaces, show a time dependence of the sorption process. Information on the related air/vapor velocity in the measuring chamber was not provided.

In Section 1.4.6.4, the question was asked at the beginning: Can one really assume that the sorption film thicknesses at the pore walls to be expected in the water-filled pore region correspond to the vapor pressure-dependent adsorption film thicknesses that are present in the open pore fraction not yet filled with water?

From the present book section and the preceding Sections 1.4.6.4 and 1.4.6.5, **it is now clear that there is no correlation between the sorptive film thicknesses in these two regions.** Films from vapor sorption with thicknesses of up to about 1.7 [nm] can be expected at high RH, while in the water-filled region films formed on the pore walls have a structure deviating from bulk water up to thicknesses of at most about 0.70 [nm], and which exhibit ice-crystalline properties at thicknesses ≤ about 0.45 [nm]. According to previous findings, this is true for hydrophilic interfaces to pure water or aqueous electrolyte solutions with concentrations ≤ approx. 1M.

For higher concentrated aqueous electrolyte solutions, significantly higher film thicknesses must be assumed, compare [68].

The analyses of ion concentrations in the pore solution of HCP from Portland cements according to EN-197 yield concentrations of at most ≈ 0.30M, compare Lothenbach et al. [69] and Kenny/Katz [70]. The vast majority of ions in the hydrated state of the cements consist of potassium and sodium ions. The ion concentration in hydrated hardened cement paste decreases drastically when increasing amounts of fly ash are used [70].

From the experimental studies, especially by G. Zhao et al. [53], it appears that mutual compression from opposing surfaces makes the adsorption films thinner, but they apparently adopt an even more stable consistency.

Therefore, the question is to be asked whether, for example, the **decrease in permeability during a pressure test** with high pressures when determining the hydraulic conductivity can also be attributed to a parallel solidification of formed adsorption films, compare Section 3.1.8.1.

1.4.8 Influence of Adsorption Films on Meniscus Formation and on Capillary Pressure in Capillary Pores

In Section 1.3, the basic relationships of fluid uptake in porous materials as a result of surface energetic conditions were discussed. A distinction was made between fluid uptake due to capillary suction and fluid storage due to condensation from the penetrating vapor phase. The investigations in the previous sections showed that **different adsorption layer thicknesses can form behind a meniscus in the water-filled pore region and in front of the meniscus**, which meet each other in the region of the meniscus.

At $\varphi = 50\%$, according to Section 1.4.6.5, an adsorption film thickness of about 0.7 [nm] is present behind the meniscus, while in front of the meniscus, the adsorption film thickness from the vapor phase is about 0.50 [nm] (**Figure 1.28a**). This raises the question of the **consequences for the formation of the meniscus and its edge angle to the pore surface**, and thus for an influence on the capillary pressure. Related to this is the question of fluid storage potential by suction or capillary condensation.

Numerous publications have investigated **what shape the fluid surface of a meniscus takes at the transition to the pore wall**. Cited here are only the papers by Churaev et al. [52] and Kuchin and Starov [72], from which **Figure 1.40a,b** were taken.

In Figure 1.40a, the shape of the menisci at complete wetting (2) and partial wetting (1) with associated edge angle is given in the figure scale. Furthermore, an adsorption film h_e at the pore inner surface of thickness 1.85 [nm] is assumed there. This is a film thickness present at the basic isotherms for flat surfaces used here at a relative vapor pressure of $\varphi \approx 99\%$ (compare **Figure 1.27**). The corresponding calculated shapes of the liquid surface at the transition of the meniscus to the pore wall are given in detail for the partial wetting case in **Figure 1.40b**.

Particularly in the presence of larger film thicknesses of, for example, $t = 1.5$ [nm] (in front of the meniscus), the question remains, despite the theoretical modeling results of Kuchin (**Figure 1.40b**), for example, to what extent a force transfer from a meniscus to the pore wall in the longitudinal direction of the pores into the membrane surface of the film may be assumed.

This mainly concerns situations where liquids are transported by capillary suction in a pore system whose pore walls are covered by said liquid film. It must be taken into account that the liquid molecules below the film surface are largely in the bulk state in the case of thicker films. Notable forces in the form of shear stresses cannot

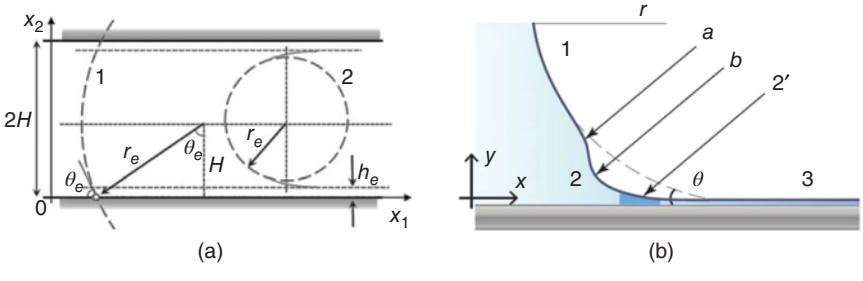

Figure 1.40 Figures and results of modeling from Kuchin et al. [71] and Kuchin and Starov [72]. (a) Representation of the shape of the menisci in total wetting (2) and in partial wetting with the corresponding contact angle θ_e. (1) (b) Liquid profile **in a capillary in the case of partial wetting** in the state of local equilibrium at excess pressure $P \neq Pe$; r and θ are the radius of the spherical meniscus in the central part of the capillary and the new local equilibrium contact angle ($\theta \neq \theta e$) (1) Spherical meniscus of a new radius r, where $r \neq re$; (2) profile of part of the transition zone at local equilibrium with the meniscus; (3) flat equilibrium liquid film of thickness he, with old equilibrium excess pressure Pe; (2') a flow zone inside the transition region. Source: Kuchin et al. [71] and Kuchin and Starov [72]/American Chemical Society.

be transmitted to the pore wall in this region, if the results of research work are interpreted accordingly.

According to the results, for example of [73], [74], and [75], when shear stresses are applied, **slipping takes place between the film surface and the firmer approximately 2 molecule-layer-thick layer** on the material surface. Only when approaching the pore wall does the surface free energy in the adsorbed film increase according to the Sections 1.4.7, 1.4.6.1, or 1.4.6.4, and thus the ability to absorb the edge stress from the meniscus.

This is also clear in the approaches to disjoining pressure in adsorption films by, for example, Churaev et al. [52] and Kuchin et al. [71]. Also, Schimmele et al. [76] assumes that, especially at contact angles $\geq 0^o$, the meniscus edge force is introduced into the "load-bearing" pore wall.

From this, the assumption could be derived that the force transfer from a meniscus in the mentioned transport situation (with the occurring molecular slipping) is always transferred into the "solidly" adsorbed surface layer about 2 molecule layers thick, according to **Figure 1.41a,b**.

Systematic investigations of this question on capillaries with different inner film thicknesses, generated from different relative humidities of air, have probably not been realized so far because of experimental difficulties.

Behavior as assumed in **Figure 1.41a,b**, on the other hand, could be **unjustified in the case of capillary condensation in pore systems**, where increasing pore filling occurs not by suction but by condensation from the vapor phase. In this case, a stress equilibrium between meniscus edge force and pore-film surface is conceivable in the region of the meniscus transition, depending on local conditions, without any appreciable effect of a slipping influence.

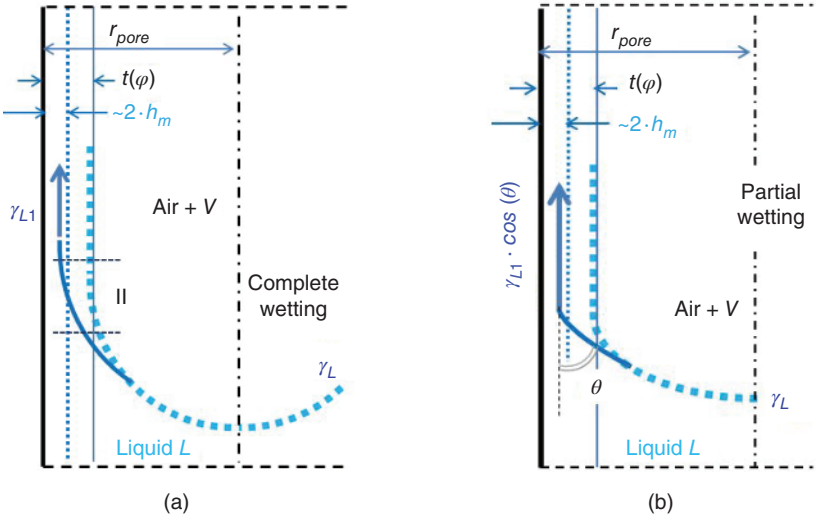

Figure 1.41 Modeling of the force transmission from the meniscus edge into the area of the contact zone. (a) Complete wetting with contact angle $\theta \approx 0^o$. (b) Partial wetting with contact angle $\theta \geq 0^o$.

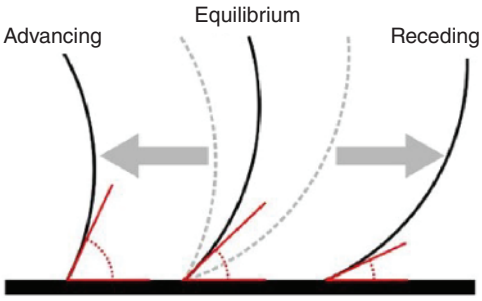

Figure 1.42 Schematic illustrated behavior of the shape of the menisci and the contact angles in a pore system during fluid adsorption (advancing meniscus) or fluid desorption (receding meniscus). Source: Andrew et al. [78]/with permission of Elsevier.

However, compared to equilibrium, a flattening of the meniscus takes place in the case of water absorption by vapor sorption and an increase of the curvature in the case of drying processes. Many publications attempt to model this process, see Starov and Velarde [77] and Kuchin and Starov [72]. Measured values on the phenomenon are reproduced, for example, in [78] and [79].

With capillary fluid uptake, a flatter meniscus and larger edge angle usually establishes itself because of the lower initial transport resistance, which transitions to the equilibrium position when transport stops. The degree of change of the edge angle depends on the particular transport resistance, see Popescu et al. [80] and **Figure 1.42**, for instance. Many publications are concerned with this question resp. the **shape of the meniscus and the contact angle as a function of liquid uptake or liquid release** in the pore system.

Different capillary pressures are associated with each of these meniscus shapes, which can differ significantly in the adsorption and desorption phases. Nevertheless, no influence on the hysteretic behavior of the moisture storage can be derived from these transient phases, since the respective equilibrium states are assigned to this behavior with the associated stationary menisci and contact angles. The condensate volume at the inner pore surfaces of the pore system forms according to Section 1.4, and because of the small influence of the discussed relation on the pore radii, **the dependencies between pore radius and capillary pressure or of Section 1.3 should be applied unchanged**.

References

1 Thommes, M., Kaneko, K., Neimark, A.V. et al. (2015). Physisorption of gases, with special reference to the evaluation of surface area and pore size distribution (IUPAC Technical Report). *Pure and Applied Chemistry* 87: 160.

2 Fagerlund, G. (2004). A Service Life Model for Internal Frost Damage in Concrete. Division of Building Materials. *Report TVBM*; Vol. 3119. Lund University.

3 Eriksson, D., Gasch, T., and Ansell, A. (2018). A hygro-thermo-mechanical multiphase model for long-term water absorption into air-entrained concrete. *Transport in Porous Media* 20: 573.

4 Carmeliet, J. and Roels, S. (2002). Determination of the moisture capacity of porous building materials. *Journal of Building Physics* 25: 209–237.

5 Krus, M. (1996). Moisture transport and storage coefficients of porous mineral building materials: theoretical principles and new test methods. *Reprint Dissertation (Stuttgart University) by Fraunhofer IRB Verlag*.

6 Scheffler, G.A. (2008). Validierung hygrothermischer Materialmodellierung unter Berücksichtigung der Hysterese der Feuchtespeicherung. Dissertation.Technische Universitt Dresden.

7 Espinosa, R.M. and Franke, L. (2006). Inkbottle Pore-Method: prediction of hygroscopic water content in hardened cement paste at variable climatic conditions. *Cement and Concrete Research* 36: 1954–1968.

8 Feldman, R.F. and Sereda, P.J. (1968). A model for hydrated Portland cement paste as deduced from sorption-length change and mechanical properties. *Materiaux et Constructions* 1: 509–520.

9 Ahlgren, L. (1972). Moisture Fixation in Porous Building Materials. *Report 36*. The Lund Inst. of Technology.

10 Welcome to DataPhysics-Instruments (2019). *Collection of Surface-Tension values of Liquids and Solids*. www.dataphysics-instruments.com (accessed 27 December 2023).

11 Pérez-Díaz, J.L., Álvarez-Valenzuelab, M.A., and García-Pradab, J.C. (2012). The effect of the partial pressure of water vapor on the surface tension of the liquid water–air interface liquid water–air interface. *Journal of Colloid and Interface Science* 381 (1): 180–182.

12 Portuguez, E., Alzina, A., Michaud, P. et al. (2017). Evolution of a water pendant droplet: effect of temperature and relative humidity. *Natural Science* 9: 1–20.

13 Chen, H., Li, Z., Wang, F. et al. (2017). Extrapolation of surface tensions of electrolyte and associating mixtures solutions. *Chemical Engineering Science* 162: 10–20.

14 Kinloch, A.J. (1980). Review the science of adhesion Part 1 : Surface and interfacial/aspects. *Journal of Materials Science* 15: 2141–2166.

15 van Honschoten, J.W., Brunets, N., and Tas, N.R. (2010). Capillarity at the nanoscale. *Chemical Society Reviews* 39: 1096–1114.

16 Barnat-Hunek, D. and Smarzewski, P. (2015). Surface free energie of hydrophobic coatings of hybrid-fiber-reinforced high-performance concrete. *Materiali in Tehnologije / Materials and Technology* 49: 895–902.

17 Kumikov, V.K. and Khokonov, K.B. (1983). On the measurement of surface free energy and surface tension of solid metals. *Journal of Applied Physics* 54: 1346–1350.

18 Yuan, Y. and Lee, T.R. (2013). Contact angle and wetting properties. In: *Surface Science Techniques*, *Springer Series in Surface Sciences 51*. Springer.

19 Lauth, G.-J. and Kowalczyk, J. (2016). *Einführung in die Physik und Chemie der Grenzflächen und Kolloide. Experimentelle Methoden: Messung der Grenzflächenspannung*. Springer-Spektrum.

20 Cwikel, D., Zhao, Q., Liu, C. et al. (2010). Comparing contact angle measurements and surface tension assessments of solid surfaces. *Langmuir* 26 (19): 15289–15294.

21 Extrand, C.W. and Moon, S.I. (2012). Which controls wetting? Contact line versus interfacial area: simple experiments on capillary rise. *Langmuir-Journal of the American Chemical Society* 28: 15629–15633.

22 Matsuoka, H., Fukui, S., and Kato, T. (2002). Nanomeniscus forces in undersaturated vapors: observable limit of macroscopic characteristics. *Langmuir* 18: 6796–6801.

23 Kim, S., Kim, D., Kim, J. et al. (2018). Direct evidence for curvature-dependent surface tension in capillary condensation: Kelvin equation at molecular scale. *Physical Review X* 8: 041046.

24 Blokhuis, E.M. and Kuipers, J. (2006). Thermodynamic expressions for the Tolman length. *Journal of Chemical Physics* 124: 74701.

25 Eslami, F. and Elliott, J.A.W. (2019). Gibbsian thermodynamic study of capillary meniscus depth. *Scientific Reports* 9: 657.

26 Maris, H. and Balibar, S. (2000). Negative pressures and cavitation in liquid helium. *Physics Today, American Institute of Physics* 53 (2): 29–34.

27 Caupin, F., Arvengas, A., Davitt, K. et al. (2012). Exploring water and other liquids at negative pressure. *Journal of Physics: Condensed Matter* 24: 284110

28 Israelachvili, J.N. (2011). *Intermolecular and Surface Forces*, 3e. Elsevier.

29 Rouquerol, F., Rouquerol, J., and Sing, K.S. (2014). *Adsorption by Powders and Porous Solids, Principles, Methodology and Applications*. Elsevier.

30 Adolphs, J. and Setzer, M.J. (1996). A model to describe adsorption isotherms. *Journal of Colloid and Interface Science* 180: 70–76.

31 Brunauer, S., Emmett, P.H., and Teller, E.J. (1938). Adsorption of gases in multimolecular layers. *Journal of the American Chemical Society* 60: 309.

32 Badmann, R., Stockhausen, N., and Setzer, M.J. (1981). The statistical thickness and the chemical potential of adsorbed water films. *Journal of Colloid and Interface Science* 82: 534–542.

33 Zandavi, S.H. and Ward, C.A. (2014). Clusters in the adsorbates of vapours and gases: Zeta isotherm approach. *Physical Chemistry Chemical Physics* 16: 10979–10989.

34 Zandavi, S.H. (2015). Vapours adsorption on non-porous and porous solids: Zeta Adsorption Isotherm Approach. Dissertation.University of Toronto.

35 Funk, M. (2012). Hysteresis der Feuchtespeicherung in porösen Materialien. Dissertation. Technische Universitt Dresden.

36 deBoer, J.H., Linsen, B.G., and Osinga, T.J. (1965). Studies on pore systems in catalysis. VI. The universal t-curve. *Journal of Catalysis* 4(6): 643–648.

37 Snoeck, D., Velasco, L.F., Mignon, A. et al. (2014). The influence of different drying techniques on the water sorption properties of cement-based materials. *Cement and Concrete Research* 64: 54–62.

38 Kumar, A., Ketel, S., Vance, K. et al. (2014). Water vapor sorption in cementitious materials—measurement, modeling and interpretation. *Transport in Porous Media* 103: 69–98.

39 Brunauer, S., Skalny, J., and Bodor, E.E. (1969). Adsorption on nonporous solids. *Journal of Colloid and Interface Science* 30: 546–552.

40 Pavlik, Z., žumár, J., Medved, I., and Černý, R. (2012). Water vapor adsorption in porous building materials: experimental measurement and theoretical analysis. *Transport in Porous Media* 91: 939–954.

41 Adolphs, J. and Setzer, M.J. (1996). Energetic classification of adsorption isotherms. *Journal of Colloid and Interface Science* 184: 443–448.

42 Adolphs, J. and Setzer, M.J. (1998). Description of gas adsorption isotherms on porous and dispersed systems with the excess surface work model. *Journal of Colloid and Interface Science* 207: 349–354.

43 Ridgway, C.J., Schoelkopf, J., Matthews, G.P. et al. (2001). The effects of void geometry and contact angle on the absorption of liquids into porous calcium carbonate structures. *Journal of Colloid and Interface Science* 239: 417–431.

44 Wu, C., Zandavi, S.H., and Ward, C.A. (2014). Prediction of the wetting condition from the Zeta adsorption isotherm. *Physical Chemistry Chemical Physics* 16: 25564–25572.

45 Churaev, N., Starke, G., and Adolphs, J. (2000). Isotherms of capillary condensation influenced by formation of adsorption films. *Journal of Colloid and Interface Science* 221: 246–253.

46 Mattia, D., Starov, V., and Semenov, S. (2012). Thickness, stability and contact angle of liquid films on and inside nanofibres, nanotubes and nanochannels. *Journal of Colloid and Interface Science* 384 (1): 149–156.

47 Li, J., Li, X., Wu, K. et al. (2016). Water sorption and distribution characteristics in clay and shale: effect of surface force. *Energy Fuels* 30: 8863–8874.

48 Teletzke, G.F. and Davis de L.E. Scriven, H.T. (1988). Wetting hydrodynamics. *Physical Review Applied* 23: 989–1007.

49 Kruk, M. and Jaroniec, M. (2002). Determination of mesopore size distributions from argon adsorption data at 77 K. *Journal of Physical Chemistry B* 106: 4732–4739.

50 Zhang, Y., Ouyang, X., and Yang, Z. (2019). Microstructure-based relative humidity in cementitious system due to self-desiccation. *Materials* 12: 1214.

51 Dash, J.G. and Peierls, R. (1982). Characteristics of adsorbed films. *Physical Review B* 25: 8.

52 Churaev, N.V., Setzer, M.J., and Adolphs, J. (1998). Influence of surface wettability on adsorption isotherms of water vapor. *Journal of Colloid and Interface Science* 197: 327–333.

53 Zhao, G., Tan, Q., Xiang, L. et al. (2015). Structure and properties of water film adsorbed on mica surfaces. *Journal of Chemical Physics* 143: 104705.

54 Xu, S., Simmons, G.C., Mahadevan, T.S. et al. (2009). Transport of water in small pores. *Langmuir* 25: 5084–5090.

55 Gruener, S., Hofmann, T., Wallacher, D. et al. (2009). Capillary rise of water in hydrophilic nanopores. *Physical Review E-APS* 79: 1–5.

56 Wu, K., Chen, Z., Li, J. et al. (2017). Wettability effect on nanoconfined water flow. *Proceedings of the National Academy of Sciences of the United States of America* 114 (13): 3358–3363.

57 Antognozzi, M., Humphris, A.D.L., and Miles, M.J. (2001). Observation of molecular layering in a confined water film and study of the layers viscoelastic properties. *Applied Physics Letters* 78 (3): 300–302.

58 Arai, T., Sato, K., Iida, A., and Tomitori, M. (2017). Quasi-stabilized hydration layers on muscovite mica under a thin water film grown from humid air. *Scientific Reports* 7: 4054.

59 Aktulga, H.M., Fogarty, J.C., Pandit, S.A., and Grama, A.Y. (2012). Parallel reactive molecular dynamics: numerical methods and algorithmic techniques. *Parallel Computing* 38: 245–259.

60 Farah, K., Müller-Plathe, F., and Böhm, M.C. (2012). Classical reactive molecular dynamics implementations: state of the art. *ChemPhysChem* 13: 1127–1151.

61 Castrillon, S.R.-V., Giovambattista, N., Aksay, I.A., and Debenedetti, P.G. (2011). Structure and energetics of thin film water. *Journal of Physical Chemistry C* 115: 4624–4635.

62 Israelachvili, J., Min, Y., Akbulut, M. et al. (2010). Recent advances in the surface forces apparatus (SFA) technique. *Reports on Progress in Physics* 73: 036601.

63 Peng, J., Guo, J., Ma, R., and Jiang, Y. (2022). Water-solid interfaces probed by high-resolution atomic force microscopy. *Surface Science Reports* 71: 100549.

64 Fukuma, T. (2015). Mechanism of atomic force microscopy imaging of three-dimensional hydration structures at a solid-liquid interface. *Physical Review B* 92: 155412.

65 Monroe, J., Barry, M., DeStefano, A. et al. (2020). Water structure and properties at hydrophilic and hydrophobic surfaces. *Annual Review of Chemical and Biomolecular Engineering* 11: 523–557.

66 Asay, D.B. and Kim, S.H. (2005). Evolution of the adsorbed water layer structure on silicon oxide at room temperature. *Journal of Physical Chemistry B* 109: 16760–16763.

67 Kimura, K., Ido, S., Oyabu, N. et al. (2010). Visualizing water molecule distribution by atomic force microscopy. *Journal of Chemical Physics* 132: 194705.

68 Martin-Jimenez, D., Chacon, E., Tarazona, P., and Garcia, R. (2016). Atomically resolved three-dimensional structures of electrolyte aqueous solutions near a solid surface. *Nature Communications* 7: 12164.

69 Lothenbach, B., Winnefeld, F., Alder, C. et al. (2007). Effect of temperature on the pore solution, microstructure and hydration products of Portland cement pastes. *Cement and Concrete Research* 37: 483–491.

70 Kenny, A. and Katz, A. (2020). Cement composition's effect on pore solution composition and on electrochemical behavior of reinforcing steel. *Israel Institute for Technology, Haifa, Israel, Reprint*.

71 Kuchin, I.V., Matar, O.K., Crasterc, R.V., and Starov, V.M. (2014). Modeling the effect of surface forces on the equilibrium liquid profile of a capillary meniscus. *Soft Matter* 10: 6024–6037.

72 Kuchin, I.V. and Starov, M. (2016). Hysteresis of the contact angle of a meniscus inside a capillary with smooth, homogeneous solid walls. *Langmuir* 32: 5333–5340.

73 Zhang, T., Li, X., Sun, Z. et al. (2017). An analytical model for relative permeability in water-wet nanoporous media. *Chemical Engineering Science* 174: 1–12.

74 Wang, F.-C. and Zhao, Y.-P. (2011). Slip boundary conditions based on molecular kinetic theory: the critical shear stress and the energy dissipation at the liquid–solid interface. *Soft Matter* 7: 8628–8634.

75 Feng, D., Li, X., Wang, X. et al. (2018). Capillary filling of confined water in nanopores: coupling the increased viscosity and slippage. *Chemical Engineering Science* 186: 228–239.

76 Schimmele, L., Napiórkowski, M., Dietrich, S. et al. (2007). Conceptual aspects of line tensions. *Journal of Chemical Physics* 127: 164715.

77 Starov, V.M. and Velarde, M.G. (2009). Surface forces and wetting phenomena. *Journal of Physics: Condensed Matter* 21: 464121.

78 Andrew, M., Bijeljic, B., and Blunt, M.J. (2014). Pore-scale contact angle measurements at reservoir conditions using X-ray microtomography. *Advances in Water Resources* 68: 24–31.

79 Siebold, A., Walliser, A., Nardin, M. et al. (1997). Capillary rise for thermodynamic characterization of solid particle surface. *Journal of Colloid and Interface Science* 186: 60–70.

80 Popescu, M.N., Ralston, J., and Sedev, R. (2008). Capillary rise with velocity-dependent dynamic contact angle. *Langmuir* 24: 12710–12716.